

<sup>1</sup>Yang Wu  
<sup>1</sup>Lei Wu  
<sup>1</sup>Fen Tang  
<sup>1</sup>Bo Wang  
<sup>1,\*</sup> Yaofeng Su

## Geo-positioning Method of Optical Satellite Unconventional Stereo Imagery Based on Optimal Intersection



**Abstract:** - Generally, the classic three-dimensional (3D) geometric positioning of optical satellite imagery uses the least squares principle to calculate the coordinates of a ground point by minimizing the sum of the squares of the distances between two imaging rays, which requires the standard stereo data with good imaging geometric conditions. As for unconventional stereo images, the undesirable and ubiquitous weak intersection phenomena exist in data will lead to bad results or even calculation failures for the conventional method. By selecting the highest precision intersection point in block adjustment, a new method that can solve the 3D coordinates with higher accuracy and stability was proposed. Tests of two data sets covering different landscapes validated the effectiveness of the method. The results showed that the geo-positioning performance and robustness of the proposed method was better than that of the conventional method, and this advantage is even greater in areas with more undulating terrain and more images with weak convergence.

**Keywords:** Geo-positioning; Unconventional stereo imagery; Block adjustment; Optimal intersection.

### I. INTRODUCTION

Since 2010, China's Earth observation technology has seen rapid development under the impetus of the "Major Project of High-Resolution Earth Observation System", especially in optical remote sensing satellites with mapping capabilities, which have become a crucial means for acquiring basic geographic spatial information[1]. 3D geometric information forms the foundation for all the information carried by high-resolution satellite remote sensing images, and the precision of geometric positioning is a core indicator of the application efficacy and advancement of high-resolution satellite remote sensing systems. Given its significance, despite geometric positioning being a key technology researched for a long time in the field of photogrammetry, many scholars are still exploring how to extract more precise 3D information using satellite images. For satellite platforms, most studies currently utilize standard stereo images formed from data collected at fixed observation angles by two or three sensors on the same satellite for geometric positioning[2][3]. However, with the development of the earth observation system from the traditional single satellite mode to the multi-satellite constellation observation mode, there will be an increasing amount of data acquired from different platforms and sources, which will exhibit significant variations in observation modes. If geometric positioning can only be conducted using standard stereo images with good convergence conditions, it will cause a substantial waste of data resources. Therefore, how to effectively use unconventional stereo images formed from multi-source satellite data for geometric positioning and to enhance its precision has great practical significance for improving the application benefits of satellite remote sensing data.

### II. RELATED WORK

Many experts and scholars have been exploring joint-positioning of multi-source images. Toutin from Canada Centre for Mapping and Earth Observation developed a positioning model applicable to multi-sensor images, which is composed of a set of independent parameters represented by several related geometric variables[4][5]. This model differs in form from the general rigorous models and theoretically requires only three ground control points (GCPs) to solve all parameters, achieving combined positioning of multi-sensor images. However, the disadvantage of this model is the necessity of GCPs. Scholars such as Li and Jeong have analyzed in detail the factors affecting the geometric positioning accuracy of heterogeneous satellite images using IKONOS, GeoEye, WorldView and other satellites[6],[7],[8]. They identified the intersection angle between imaging light rays as the most crucial factor affecting 3D positional errors and have verified the feasibility of high-precision joint positioning of multi-source satellite images through experiments with various combinations of heterogeneous data pairs. Qin conducted geometric correction and bundle block adjustment experiments on multi-source

<sup>1</sup> College of Information and Communication, National University of Defense Technology, Wuhan 430010, China

\*Corresponding author: Yaofeng Su

Copyright © JES 2024 on-line : journal.esrgroups.org

satellite images including optical push-broom and synthetic aperture radar using the Rational Function Model (RFM) and its extended models[9]. The experiments fully verified that the proposed extended RFM model can be used for geometric processing of multi-source satellite remote sensing images. Based on the principles of photogrammetry and corresponding mathematical theories, Wang uses the combination of RFM model, collinear equation model and affine transformation model to achieve the composite positioning of multi-source images for the same area images taken by different sensors or cameras. Xing established and verified the correctness of the bundle adjustment model for optical and radar images[11]. On this basis, they analyzed the influence of the distribution, quantity, and precision of GCPs on the positioning results. Cheng has modified and reconstructed the imaging equations and positioning models of existing aerial, aerospace optics and radar remote sensing images, achieving joint positioning of multi-source heterogeneous remote sensing images with rare or no GCPs[12],[13]. Yan performed combined block adjustment experiments on SPOT images of the same source but different resolutions, indicating that the number of GCPs is not the more the better[14]. Chen proposed two block adjustment modes[15]. The first type utilizes digital elevation model (DEM) to locate a single image, followed by compensation for the inconsistency in coordinates of tie points (TPs) between images. The second type involves the simultaneous positioning of all images. When the image resolutions are similar, the positioning accuracy of both methods is comparable; however, when the resolutions differ, the second method yields higher positioning accuracy. Zhang proposed the combined adjustment with linear array and frame array imagery (CALFI) method, in which a revised recursive partitioning technique is utilized to solve the large normal matrix[16]. The experimental results on simulated data show that both the accuracy and the condition index of the CALFI model are superior to the conventional bundle adjustment model with either linear array or frame array imagery separately due to the higher redundancy. Dai explored the feasibility and positioning accuracy of block adjustment for P5 and WorldView-1 satellite imagery based on RFM under conditions of minimal control and weak connections[17]. The results indicate that even with weak connections, the technique of block adjustment for satellite imagery remains applicable and yields high positional accuracy. Xu have experimentally demonstrated that the joint adjustment of ZY3 satellite imagery and TH1 imagery could meet the mapping accuracy of 1:50,000[18]. Li and Tong have proven through experimentation that the positioning accuracy of low-resolution images can be improved by integrating them with high-resolution images[19],[20]. Wu focused on densely populated urban areas as their study regions, utilizing advantage of the high planimetric accuracy of aerospace imagery and the high elevation accuracy of LiDAR imagery to improve the positioning accuracy through the integrated application of these two types of imagery[21]. Li introduced four typical cases of large-scale adjustment, including large-scale BA without GCPs for optical stereo satellite images, large-scale BA with laser altimetry data for optical stereo satellite images, large-scale BA for UAV oblique photogrammetry, and large-scale BA for indoor photogrammetry in caves with a large number of close-range images[22].

From the above, it can be seen that current research on multi-source image geometric positioning mainly focuses on sensor types, imaging models, control data, etc. Most of the related studies only focuses on the analysis of the phenomena presented by heterogeneous satellite data. However, the accuracy of stereo data positioning is also closely related to the geometric configuration between images. For unconventional stereo images composed of randomly integrated different sensor data, existing methods may not always be applicable. In response to this situation, from the perspective of stereo data geometry, we propose a high-precision geometric positioning method which could be robustly applied to unconventional stereo images composed of random combinations of various optical sensor data, and analyze its effectiveness through experiments.

### III. PROPOSED APPROACH

#### A. Classic positioning method and its error analysis

The geometric schematic diagram of positioning using overlapping images is shown in Figure 1. In the Figure 1, *Scene-1* and *Scene-2* are two images with overlapping areas,  $P_{true}$  is the true position of a certain point on the ground,  $P_{ray-1}$  and  $P_{ray-2}$  are imaging rays for  $P_{true}$  from *Scene-1* and *Scene-2* respectively,  $P_1$  and  $P_2$  are the intersection points on the two imaging rays at the same elevation as  $P_{true}$ .  $A, B, C$  are candidate intersection points, and  $P_A, P_B, P_C$  are their projection points on the elevation plane  $P_{true}$ . Ideally, the orientation of two imaging rays should be precise and unbiased. The position coordinates of a ground point can be determined by calculating the intersection of these two imaging ray vectors in 3D space. However, in practice,

there are inevitably pointing errors of *Scene-1* and *Scene-2* in the imaging light constructed by the sensor imaging model, which leads to the fact that these two vectors do not intersect in object space. As a result, the 3D position coordinates of the ground point exhibit both horizontal and vertical errors. In such cases, classic geometric positioning methods employ the principle of least squares for computation, that is, the position where the sum of the squares of the distances between the two vectors is minimized is designated as the calculated coordinates of the ground point. In fact, the position calculated by the least square adjustment method is the midpoint of the shortest distance line segment connecting the two vectors.

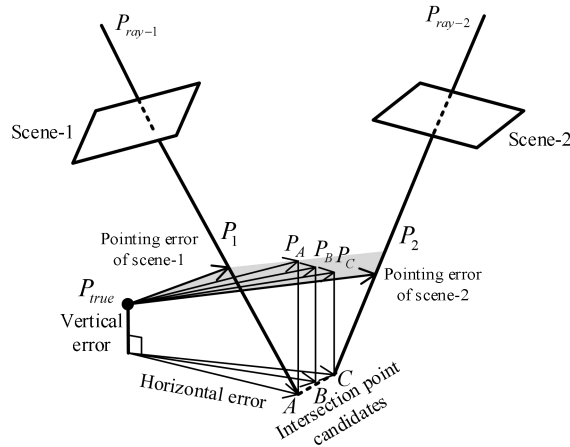


**Figure 1.** The geometric schematic diagram of 3D positioning

From the positioning method described above, the ground point is located in the vector of the shortest distance between the two imaging rays, which can be determined as the midpoint  $B$  according to the least square principle. However, this method is based on the assumption that the two images have similar pointing errors. For unconventional stereo images, the pointing errors between the two images may vary significantly, which can lead to issues when applying this method in such cases. As can be seen from Figure 1, horizontal error varies depending on the choice of location among the alternatives point  $A$ ,  $B$ , and  $C$ . Assuming that the imaging light direction accuracy of *Scene-1* is significantly higher than that of *Scene-2*, if the final 3D position is determined to be at point  $A$ , the horizontal error will be effectively reduced.

#### B. Overview of the proposed method

For the problem of applying classic methods to unconventional stereo images, a geometric positioning method based on optimal intersection is proposed in the paper, which can effectively improve the accuracy of geometric positioning of unconventional stereo images with greatly different pointing errors. It is capable of stable solutions for any configuration of overlapping images and is largely unaffected by bundle block conditions such as intersection angles. The specific process of this method is as described as follows.

Firstly, feature point detection algorithms such as SIFT or SURF are utilized to extract tie points in the overlapping areas of stereo images. Secondly, an unconventional stereo imagery model is constructed based on the original RFM imaging equations that attached to the images. Thirdly, apply the planar adjustment method described in reference[23], open-source DEM data such as SRTM is used as an elevation reference to perform a planar block adjustment, yielding error compensation parameters for the original RFM model and ground point coordinates (e.g. point  $B$  in Figure 1). Then, the RFM model is updated with the calculated error compensation parameters, and the pointing errors of the two images are computed using GCPs. Lastly, the image with the highest pointing accuracy is selected to recalculate the ground point coordinates (e.g. point  $A$  in Figure 1), that is, the finally object space 3D coordinates are computed using the image coordinates under the imaging rays with higher pointing accuracy. The workflow of the algorithm is shown in Figure 2.

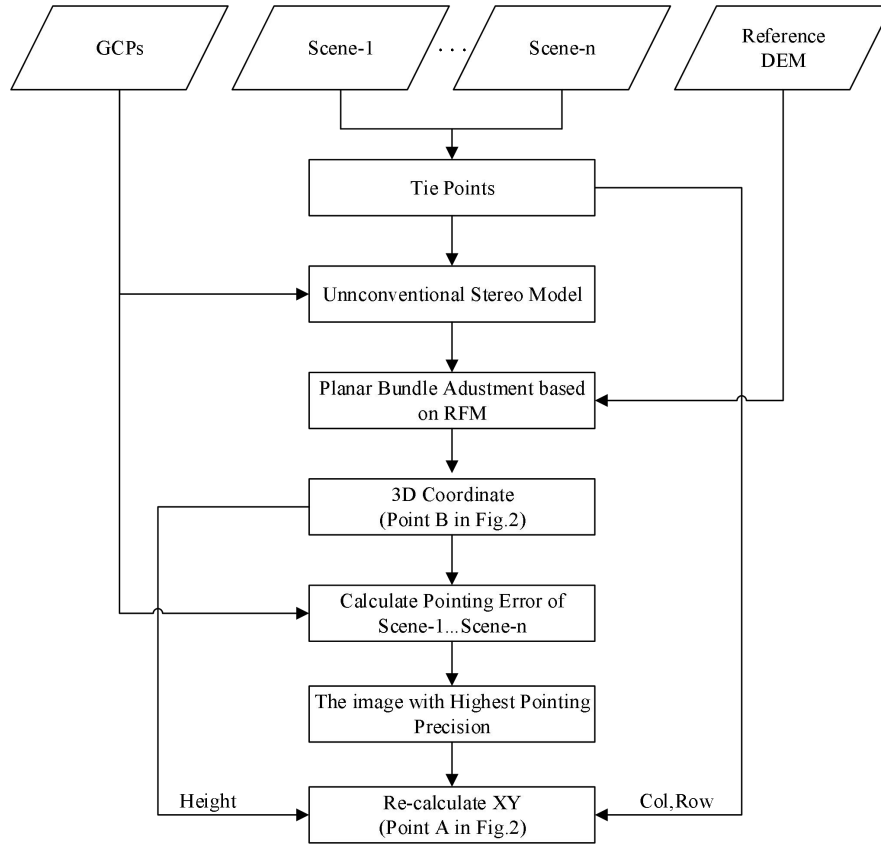


**Figure 2.** The workflow for the image geo-location based on optimal intersection

C. The rational function model

With the advantages of simple form and being sensor-independent, the RFM sensor model proposed by Grodecki and Dial [24] was used for the modeling described in this paper. Since the RFM has been fully studied in previous work, only a brief description is provided here.

The RFM uses the ratio of two cubic polynomials to describe the relationship between the image space and the object space. The model equations are expressed as Equation (1).

$$\begin{cases} s_n = \frac{Num_s(\varphi_n, \lambda_n, h_n)}{Den_s(\varphi_n, \lambda_n, h_n)} \\ l_n = \frac{Num_l(\varphi_n, \lambda_n, h_n)}{Den_l(\varphi_n, \lambda_n, h_n)} \end{cases} \quad (1)$$

where  $(s_n, l_n)$  is the normalized image coordinate;  $(\varphi_n, \lambda_n, h_n)$  is the normalized ground coordinate.

$Num_s(\varphi_n, \lambda_n, h_n)$ ,  $Den_s(\varphi_n, \lambda_n, h_n)$ ,  $Num_l(\varphi_n, \lambda_n, h_n)$ ,  $Den_l(\varphi_n, \lambda_n, h_n)$  are the third-order polynomial of the following form:

$$p = a_1 + a_2\lambda_n + a_3\varphi_n + a_4h_n + a_5\lambda_n\varphi_n + a_6\lambda_nh_n + a_7\varphi_nh_n + a_8\lambda_n^2 + a_9\varphi_n^2 + a_{10}h_n^2 + a_{11}\varphi_n\lambda_nh_n + a_{12}\lambda_n^3 + a_{13}\lambda_n\varphi_n^2 + a_{14}\lambda_nh_n^2 + a_{15}\lambda_n^2\varphi_n + a_{16}\varphi_n^3 + a_{17}\varphi_nh_n^2 + a_{18}\lambda_n^2h_n + a_{19}\varphi_n^2h_n + a_{20}h_n^3 \quad (2)$$

where  $a_i (i = 1, 2, \dots, 20)$  are the RPCs. The calculation of normalization is as follows:

$$\begin{cases} \varphi_n = (\varphi - \varphi_0) / \varphi_s \\ \lambda_n = (\lambda - \lambda_0) / \lambda_s \\ h_n = (h - h_0) / h_s \end{cases} \quad \begin{cases} s_n = (s - s_0) / s_s \\ l_n = (l - l_0) / l_s \end{cases} \quad (3)$$

where  $(\varphi, \lambda, h)$  are the geodetic longitude, latitude, and height components of the ground coordinate;  $(s, l)$  are the sample and line components of the image coordinate;  $s_0, l_0, \varphi_0, \lambda_0, h_0$  and  $s_s, l_s, \varphi_s, \lambda_s, h_s$  are the corresponding offset and scale terms.

RPCs and the normalized parameters are stored together in satellite imagery auxiliary files. To maintain numerical precision, the object and image space coordinates are normalized to  $(-1, +1)$ .

*D. The planar block adjustment*

The planar block adjustment of satellite images refers to a method where only the affine transformation parameters and planimetric coordinates of TPs are solved, while the elevation value is interpolated from the reference DEM in the iteration. In this way, the unknowns of the ground point coordinate recede from 3 to 2, so the negative effect caused by the small intersection angle can be avoided.

Due to the imperfect measurement of satellite ephemeris and attitude, the vendor-provided RPCs are commonly inaccurate. To weaken the impact of the measuring error, the most common solution is to adjust the image coordinates, but not correct the RPCs. Studies have shown that bias compensation of the affine transformation model in the image space can eliminate systematic errors. The affine transformation model is made up of polynomials of line and sample coordinates, as shown in Equation (4).

$$\begin{cases} \Delta s = e_0 + e_s \cdot s + e_l \cdot l \\ \Delta l = f_0 + f_s \cdot s + f_l \cdot l \end{cases} \quad (4)$$

where  $(\Delta s, \Delta l)$  are the differences between the measured and nominal coordinates in an image space;  $(e_0, e_s, e_l)$  and  $(f_0, f_s, f_l)$  are the bias compensation parameters; and  $(s, l)$  are the coordinates of the image point.

Adding the correction terms  $(\Delta s, \Delta l)$  in the image space by substituting Equation (4) into Equation (1) yields:

$$\begin{cases} \hat{s} = s + \Delta s = e_0 + e_1 \cdot s + e_2 \cdot l \\ \hat{l} = l + \Delta l = f_0 + f_1 \cdot s + f_2 \cdot l \end{cases} \quad (5)$$

where  $(\hat{s}, \hat{l})$  are the coordinates of the image point as measured manually,  $(s, l)$  are the coordinates of the image point as calculated with the RFM, namely:

$$\begin{cases} s = s_s \cdot \frac{Num_s(\varphi_n, \lambda_n, h_n)}{Den_s(\varphi_n, \lambda_n, h_n)} + s_0 \\ l = l_s \cdot \frac{Num_l(\varphi_n, \lambda_n, h_n)}{Den_l(\varphi_n, \lambda_n, h_n)} + l_0 \end{cases} \quad (6)$$

Then, the observation equation can be written as:

$$\begin{cases} v_s = e_0 + e_1 \cdot \left( s_s \cdot \frac{Num_s(\varphi_n, \lambda_n, h_n)}{Den_s(\varphi_n, \lambda_n, h_n)} + s_0 \right) + e_2 \cdot \left( l_s \cdot \frac{Num_l(\varphi_n, \lambda_n, h_n)}{Den_l(\varphi_n, \lambda_n, h_n)} + l_0 \right) - \hat{s} \\ v_l = f_0 + f_1 \cdot \left( s_s \cdot \frac{Num_s(\varphi_n, \lambda_n, h_n)}{Den_s(\varphi_n, \lambda_n, h_n)} + s_0 \right) + f_2 \cdot \left( l_s \cdot \frac{Num_l(\varphi_n, \lambda_n, h_n)}{Den_l(\varphi_n, \lambda_n, h_n)} + l_0 \right) - \hat{l} \end{cases} \quad (7)$$

where  $(v_s, v_l)$  are the residual errors of the image point.

By linearizing Equation (7) and expanding it to the first term, the basic error equation of the planar block adjustment can be obtained:

$$\begin{bmatrix} v_s \\ v_l \end{bmatrix} = \begin{bmatrix} \frac{\partial v_s}{\partial e_0} & \frac{\partial v_s}{\partial e_1} & \frac{\partial v_s}{\partial e_2} & \frac{\partial v_s}{\partial f_0} & \frac{\partial v_s}{\partial f_1} & \frac{\partial v_s}{\partial f_2} & \frac{\partial v_s}{\partial \varphi} & \frac{\partial v_s}{\partial \lambda} \\ \frac{\partial v_l}{\partial e_0} & \frac{\partial v_l}{\partial e_1} & \frac{\partial v_l}{\partial e_2} & \frac{\partial v_l}{\partial f_0} & \frac{\partial v_l}{\partial f_1} & \frac{\partial v_l}{\partial f_2} & \frac{\partial v_l}{\partial \varphi} & \frac{\partial v_l}{\partial \lambda} \end{bmatrix} \cdot \begin{bmatrix} \Delta e_0 \\ \Delta e_1 \\ \Delta e_2 \\ \Delta f_0 \\ \Delta f_1 \\ \Delta f_2 \\ \Delta \varphi \\ \Delta \lambda \end{bmatrix} - \begin{bmatrix} \varepsilon_s \\ \varepsilon_l \end{bmatrix} \quad (8)$$

where  $\Delta e_0, \Delta e_1, \Delta e_2, \Delta f_0, \Delta f_1, \Delta f_2$  are the corrections of the affine transformation parameters;  $(\Delta \varphi, \Delta \lambda)$  are the corrections of the plane coordinates; and  $\varepsilon_s, \varepsilon_l$  are the approximate values of the observation equation.

Equations (8) can be written in matrix form:

$$V = AX - L \quad (9)$$

where  $V$  is the residual vector of the image coordinate observation;  $A$  is a partial derivatives vector of unknowns;  $L$  is the discrepancy vector;  $X$  is the incremental vector of unknowns. It should be noted that  $X$  of a TP and a GCP are different. For a TP,  $X$  is the incremental vector of affine transformation parameters and plane coordinates; for a GCP,  $X$  is the incremental vector of affine transformation parameters.

For stereo adjustment, the initial value of the tie point is commonly determined by forward intersection. However, for images with weak convergence, this method does not work. Supported by a reference DEM and RPCs, the ray-tracing method can address this issue. The specific solution is as follows.

Step1: Use the “height-offset (normalized parameter)” value of the provided RPCs of the image as the first initial elevation value

Step2: Solve the planimetric coordinates by the DEM and RPCs of a single image;

Step3: Interpolate the new elevation value from the DEM by the planimetric coordinates solved in step 2;

Step4: Repeat steps 1–3 until the elevation difference is less than the set threshold.

For the TP existing in multiple overlapped images, calculate the ground 3D coordinates of each image by the ray-tracing method, and take the average as the initial value of the TP for planar block adjustment.

After the initial value of all unknowns are determined, then the adjustment iteration computation is performed with the support of GCPs, TPs and the DEM. The plane coordinates of the TPs in object space and bias compensation parameters will be refreshed after each iteration. Next, the DEM is adopted as the height constraint. The elevation value  $Z$  of the TP is interpolated from the DEM rather than from the intersection of multiple satellite images. Subsequently, the plane coordinates  $(X, Y)$  together with the elevation  $Z$  is set as a new ground coordinate value of the TP in the next iteration. Repeat the above procedures until the whole adjustment process has converged. It should be noted that the elevation difference between the two iterations is also one of the considerations when deciding whether to stop the iteration.

#### IV. EXPERIMENTS AND DISCUSSIONS

##### A. Test Data and Pre-processing

Two different geomorphological data sets were chosen as the study area: the Qiqihar district and the Syria district. The Qiqihar test area includes sensor data of two different platforms: TH1 and BJ2. The TH1 data consists of 12 panchromatic images from 2 tracks acquired in September 2015 and March 2016; the BJ2 data includes 4 panchromatic images from 2 tracks obtained in May 2020. The Qiqihar area is characterized by plain topography, with 44 evenly distributed GCPs within the test area. The Syria test area also encompasses data from two types of sensors: ZY3 and GF2. The ZY3 data consists of 3 images acquired in February 2018, while the GF2 data includes 1 image obtained in May 2017. The Syria area is characterized by mountainous terrain and is equipped with 17 evenly GCPs. Among the data mentioned, ZY3 and TH1 are stereoscopic mapping satellites composed of forward-looking, backward-looking, and nadir sensors, which create well-intersecting tri-stereoscopic images during Earth observation. While BJ2 and GF2 are non-mapping satellites that primarily

image the Earth by attitude maneuvers. The distribution of images and GCPs for both test areas is illustrated in Figure 3.

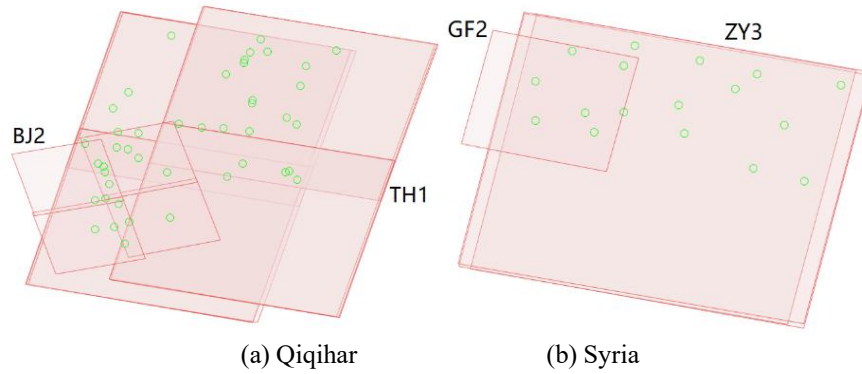


Figure 3. The sketch of ground coverage area and distribution of GCPs

To fully understand these two sets of data, the intersection angle between images was calculated using the method of the line-of-sight vector before the experiments were conducted, as shown in the figure below.

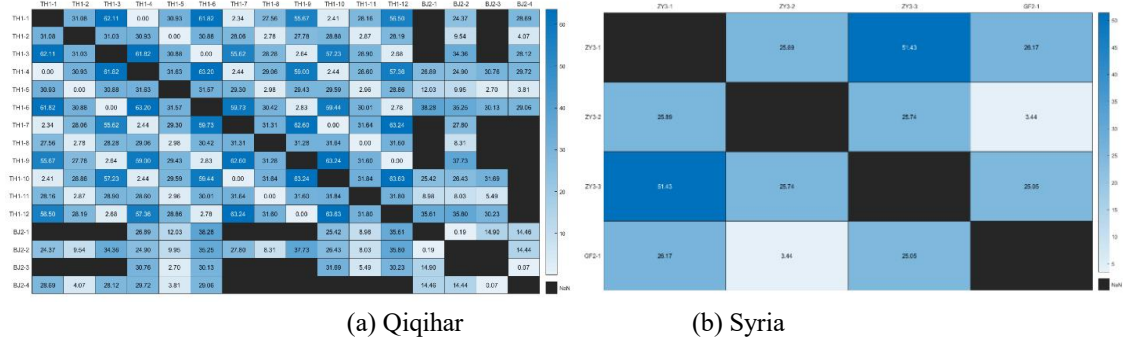


Figure 4. The intersection angles of overlapped images (the abscissa and ordinate in the figure indicate the image ID, the value in the small squares indicate the intersection angle. Black squares indicate no overlap or calculation values between images.)

As can be seen from Figure 4, the intersection angle of adjacent sensors of TH1 satellite is about 31°, the intersection angle of forward and backward sensors can reach 62°. Similar results also exist on the ZY3 satellite, with an intersection angle of 25° for adjacent sensors, and the intersection angles of forward and backward sensors can reach 51°. The intersection angle of overlapping images formed by TH1 and ZY3 are both good and met the design criteria. This good intersection angle of mapping satellite ensures the accuracy and stability of geographical mapping. Meanwhile, the BJ2 and GF2 satellites do not possess a stable stereoscopic observation structure, as images from the same sensor on the same orbit are essentially segmented from long strip data. As such, the intersection angle between same-orbit image data is approximately 0°. The inclusion of non-mapping satellite data results in weak convergence phenomena within the test area, and the data thus composed does not conventional stereo imagery. This situation can affect the stability of the bundle block adjustment, thereby affecting the accuracy of the final positioning.

It should be noted that the intersection angles in Figure 4 are based on the average values of intersection angles calculated from all homonymous tie points. Consequently, the resulting image intersection angles exhibit minor variations. The intersection angle of each homonymous ray is related to the terrain, baseline length, and flight altitude. If the terrain is relatively flat, the differences in intersection angles will not be significant; however, if the aircraft flies at a lower altitude and the ground has considerable relief, the intersection angles for different homonymous points in the same image will vary more substantially.

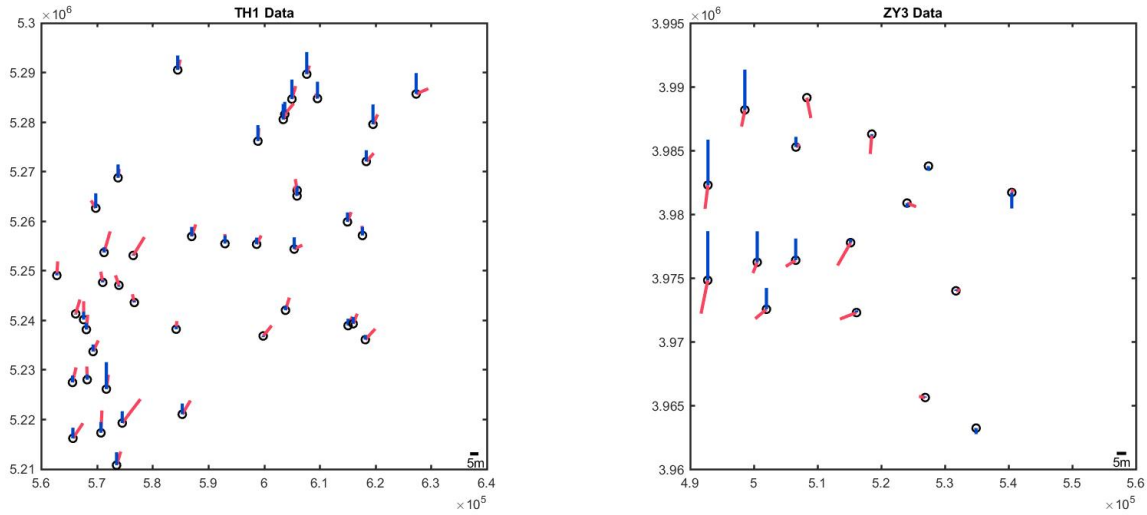
B. Positioning experiment of original single sensor data

To verify the effectiveness of the algorithm in improving accuracy, GCPs were used as independent check points (ICPs) to validate the original positioning accuracy of all sensor data. In the test, direct forward intersection method is adopted to verify the object space positioning accuracy of TH1 and ZY3 data. While BJ2 and GF2 sensor images, due to the presence of weak intersection situations, cannot perform forward intersection calculations and instead verify by re-projecting errors from the object space 3D coordinates to the image space

2D coordinates. The residual statistics of various data are shown in Tables 1 to 2. Based on the residuals value, residual distribution maps are drawn, where circular symbols represent ICPs, triangular symbols represent GCPs, red lines represent planimetric residuals, and blue lines represent elevation residuals. (Note: The accuracy assessment of object space coordinates is conducted in the UTM projection coordinate system.)

**Table 1.** Object space residual error statistics of ICPs among TH1 and ZY3 data (unit: meters)

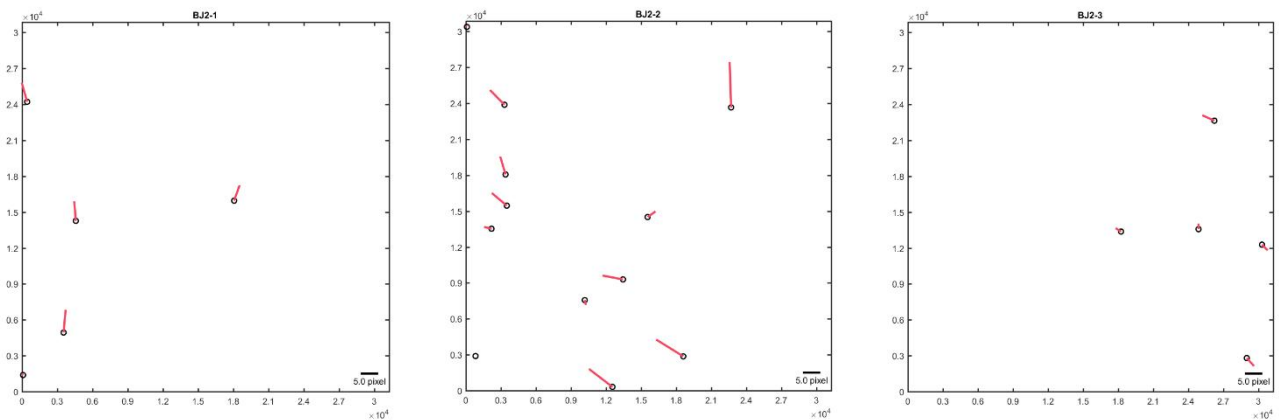
Sensors	ICPs	X			Y			Plane	Elevation		
		Mean	Max	RMS	Mean	Max	RMS	RMS	Mean	Max	RMS
TH1	44	2.638	10.868	3.468	7.881	16.030	8.383	9.072	6.473	18.136	7.702
ZY3	17	3.035	8.688	3.863	2.831	8.727	3.811	5.426	3.993	12.857	5.829



**Figure 4.** Object space residual error distribution map of ICPs among TH1 data and ZY3 data

**Table 2.** Image space residual error statistics of ICPs among BJ2 and GF2 data (unit: pixels)

Image ID	ICPs	x			y		
		Mean	Max	RMS	Mean	Max	RMS
BJ2-1	5	1.297	2.242	1.464	4.929	6.340	5.081
BJ2-2	12	3.144	7.727	4.001	3.455	12.617	4.742
BJ2-3	5	1.739	3.444	2.057	1.560	2.214	1.611
BJ2-4	7	1.635	3.957	2.150	1.296	3.859	1.752
GF2-1	6	82.366	85.367	82.391	18.097	20.558	18.166



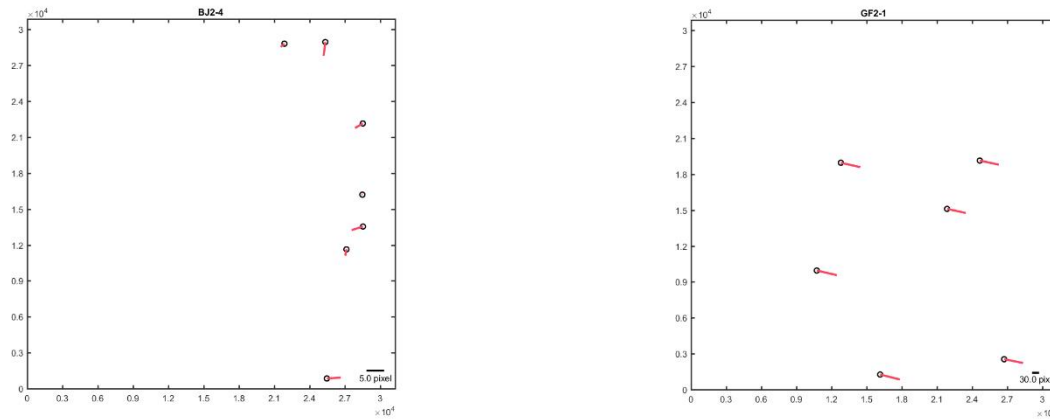


**Figure 5.** Image space residual error distribution map of ICPs among BJ2 data and GF2 data

From the above results, it can be seen that all data contain certain systematic errors, especially the GF2 data, which has a relatively large systematic error. Further processing is needed to improve accuracy.

*C. Unconventional stereo data positioning experiment*

To comprehensively validate the algorithm, geo-location experiments were conducted using both the conventional bundle block adjustment method and the proposed method. The auxiliary elevation data used in the experiments of this paper's method is the DEM data of SRTM V4.1 version. Under different numbers of GCPs, the statistical situation of the object space residuals at the ICPs is shown in Table 3 and 4.

**Table 3.** Object space residual error statistics of ICPs by the conventional method (unit: meters)

Image Type	GCPs	ICPs	X			Y			Plane	Elevation		
			Mean	Max	RMS	Mean	Max	RMS	RMS	Mean	Max	RMS
TH1+BJ2	0	44	2.438	7.050	3.192	4.885	8.405	5.260	6.153	6.301	10.549	6.762
TH1+BJ2	2	42	1.939	5.249	2.475	5.072	8.512	5.472	6.006	5.848	10.555	6.313
TH1+BJ2	4	40	1.778	3.598	2.178	4.952	8.405	5.347	5.774	5.838	10.549	6.270
TH1+BJ2	8	36	1.663	3.598	2.083	4.737	7.546	5.126	5.533	5.747	8.606	6.020
ZY3+GF2	0	17	55.345	61.312	56.551	35.289	37.334	36.132	67.108	60.923	67.927	61.107
ZY3+GF2	2	15	5.527	14.180	8.430	3.713	9.855	5.769	10.215	10.691	30.121	14.511
ZY3+GF2	4	13	4.821	13.222	7.045	4.239	9.709	5.384	8.867	2.643	22.395	10.760

**Table 4.** Object space residual error statistics of ICPs by the proposed method (unit: meters)

Image Type	GCPs	ICPs	X			Y			Plane	Elevation		
			Mean	Max	RMS	Mean	Max	RMS	RMS	Mean	Max	RMS
TH1+BJ2	0	44	1.998	6.896	2.567	3.827	8.131	4.491	5.173	7.869	18.350	8.554
TH1+BJ2	2	42	1.920	5.277	2.520	3.020	7.561	3.682	4.461	4.234	12.439	5.172
TH1+BJ2	4	40	1.917	5.525	2.539	2.572	6.606	3.080	3.992	4.075	11.609	5.039
TH1+BJ2	8	36	1.821	5.187	2.486	2.349	6.797	3.075	3.954	3.738	11.215	4.845
ZY3+GF2	0	17	1.590	16.011	6.556	1.034	7.618	4.264	7.821	1.274	5.921	3.133
ZY3+GF2	2	15	0.736	6.046	2.849	0.745	6.749	2.886	4.055	0.543	3.722	2.901
ZY3+GF2	4	13	0.892	6.552	3.217	0.667	3.960	2.406	4.017	0.532	3.716	2.878

Experimental results indicate that for unconventional stereo satellite data with weak intersection imagery, the planimetric and elevation accuracy achieved by the proposed method generally surpasses that of conventional approaches. A comparison of the experimental results from the two datasets also reveals that the precision disparity between the two methods is significantly greater in the Syrian area than in the Qiqihar area. This is attributed to the pronounced topographic undulations in the Syrian region combined with the unstable geometric relationships of bundle block caused by weak intersection imagery. These factors drastically increase the uncertainty of spatial position coordinates calculated by the conventional method. Even minimal errors can lead to substantial deviations in the 3D coordinates, resulting in a greater discrepancy between point A and point B as shown in Figure 1. This suggests that the method presented in this paper demonstrates robustness against weak intersection imagery and that its advantages over conventional methods become increasingly apparent in areas with greater topographic variation. Furthermore, in the absence of GCPs, the elevation accuracy of the Qiqihar

survey area determined by conventional methods is superior to that of the method discussed in this paper, which is primarily due to the precision of the auxiliary DEM data employed. Nonetheless, on the whole, the effectiveness of the proposed method in enhancing precision and its robustness in handling weak intersection imagery is superior to conventional methods, offering greater benefits in processing non-conventional stereo imagery.

## V. CONCLUSIONS

Optical Satellite unconventional Stereo images are ubiquitous. However, the undesirable weak convergence geometry phenomenon in unconventional Stereo images would lead to bad results or even iteration failures in the classical BBA method, which greatly limits the usage of data. To reduce the reliance on image pairs with good convergence, a novel approach, which can effectively solve the 3D coordinates even for unconventional stereo satellite imagery with weak geometric convergence, is presented in the paper. To fully validate the algorithm, two different geomorphological areas were selected and a series of tests with different purposes was implemented. These experimental results fully verified the effectiveness of the algorithm. The final results showed the plane and elevation accuracy of the proposed method is better than that of the conventional method, and this advantage is even greater in areas with more undulating terrain and more images with weak convergence. Compared with traditional methods, the proposed method has better accuracy and robustness.

## VI. REFERENCES

- [1] Li D R, Tong Q X, Li R X, et al. Current Issues in High-resolution Earth Observation Technology[J]. *Sci China Earth Sciences*, 2012, 55: 1043–1051.
- [2] Gong J Y, Wang M, Yang B. High-precision Geometric Processing Theory and Method of High-resolution Optical Remote Sensing Satellite Imagery without GCP[J]. *Acta Geodaetica et Cartographica Sinica*, 2017, 46(10): 1255-1261.
- [3] Chu G H, Ji S, Dong Y, et al. Preliminary Verification of Geometric Positioning Plane Accuracy of GF-7 Satellite Image[J]. *Journal of Geomatics*, 2023, 48(5):49-54.
- [4] Toutin T. Block Bundle Adjustment of Landsat 7 ETM+ Images over Mountainous Areas[J]. *Photogrammetric Engineering & Remote Sensing*, 2003, 69(12):1341-1349.
- [5] Toutin T. Generation of DSMs from SPOT-5 in-track HRS and across-track HRG Stereo Data using Spatiotriangulation and Autocalibration[J]. *ISPRS Journal of Photogrammetry & Remote Sensing*, 2006, 60(3):170-181.
- [6] Li R, Zhou F, Niu X, et al. Integration of Ikonos and QuickBird Imagery for Geopositioning Accuracy Analysis[J]. *Photogrammetric Engineering and Remote Sensing*, 2007, 73(9):1067-1074.
- [7] Jeong J, Kim T. Analysis of Dual-Sensor Stereo Geometry and Its Positioning Accuracy[J]. *Photogrammetric Engineering & Remote Sensing*, 2014, 80(7):653-662.
- [8] Jeong J, Yang C, Kim T. Geo-Positioning Accuracy Using Multiple-Satellite Images: IKONOS, QuickBird, and KOMPSAT-2 Stereo Images[J]. *Remote Sensing*, 2015, 7(4):4549-4564.
- [9] Qin X W, Li L, Zhang G. Multisensor Satellite Imagery Block Adjustment without GCP[J]. *Journal of Liaoning Technical University*, 2007, 26(2):187-189.
- [10] Wang W X. The 3D Reconstruction Methods Study Based on Generalized Stereopair[D]. Liaoning Technical University, 2007.
- [11] Xing S, Xu Q, Liu J, et al. Bundle Block Adjustment with Multi-source Satellite Remote Sensing Images[J]. *Acta Geodaetica et Cartographica Sinica*. 2009, 38(2):125-130.
- [12] Cheng C Q, Zhang J X, Huang G M, et al. Combined Positioning of TerraSAR-X and SPOT-5 HRS Images with RFM Considering Accuracy Information of Orientation Parameters[J]. *Acta Geodaetica et Cartographica Sinica*, 2017, 46(2): 179-187.
- [13] Cheng C, Zhang L, Yan Q, et al. An Integrated Geometric Model for Multi-source Spaceborne Optical Imagery[J]. *Journal of Tongji University (Nature Science)*, 2014, 42(7):1127-1132.
- [14] Yan L, Ma Z L. Combined Block Adjustment with Multi-resolution Satellite Remote Sensing Imagery[J]. *Remote Sensing Information*, 2015, 30(3):10-13.
- [15] Chen L C. Geometric Integration of Heterogeneous Models for Multisatellite Image Positioning[J]. *IEEE Transactions on Geoscience & Remote Sensing*, 2012, 50(7):2802-2809.
- [16] Zhang Y J, Lin L W, Zheng M T, et al. Combined Bundle Block Adjustment with Spaceborne Linear Array and Airborne Frame Array Imagery[J]. *The Photogrammetric Record*, 2013, 28(142):162-177.
- [17] Dai Q L, Zhang H W, Lin Z J. Study on Multi-satellite Images Block Adjustment of Scarce Control[J]. *Science of Surveying and Mapping*, 2014, 39(9):34-38.
- [18] Xu Y, Zhang G, Wang T Y. Joint Adjustment of ZY-3 and TH-1 Satellite Images[J]. *Geospatial Information*, 2018, 16(1):9-11.
- [19] Li R X, Deshpande S, Niu X T, et al. Geometric Integration of Aerial and High-Resolution Satellite Imagery and Application in Shoreline Mapping[J]. *Marine Geodesy*, 2008, 31(3):143-159.

- [20] Tong X H, Liu S J, Xie H, et al. Geometric Integration of Aerial and QuickBird Imagery for High Accuracy Geopositioning and Mapping Application: A Case Study in Shanghai[J]. *Marine Geodesy*, 2010, 33(4):437-449.
- [21] Wu B, Tang S J, Zhu Q, et al. Geometric Integration of High-resolution Satellite Imagery and Airborne LiDAR Data for Improved Geopositioning Accuracy in Metropolitan Areas[J]. *ISPRS Journal of Photogrammetry & Remote Sensing*, 2015, 109:139-151.
- [22] Li D R, Yang B, Wang B, et al. Large-scale Automatic Block Adjustment from Satellite to Indoor Photogrammetry[J], 2023;26(2): 1-15.
- [23] Wu Y, Zhang Y S, Wang D H, et al. Optical Satellite Image Geo-Positioning with Weak Convergence Geometry[J]. *ISPRS International Journal of Geo-information*, 2018, 7(7):251.
- [24] Grodecki J; Dial G. Block Adjustment of High-Resolution Satellite Images Described by Rational Polynomials[J]. *Photogrammetric Engineering & Remote Sensing*, 2003, 69, 59–70.